New Journal of Physics
The open access journal at the forefront of physics

Deutsche Physikalische Gesellschaft DPG IOP Institute of Physics

PAPER • OPEN ACCESS

Ultrathin Co films with Pt and Au covers—magnetic and structural properties driven by Ga^+ ion irradiation

To cite this article: P Mazalski *et al* 2021 *New J. Phys.* **23** 023015

New Journal of Physics
The open access journal at the forefront of physics

Deutsche Physikalische Gesellschaft DPG
IOP Institute of Physics

Published in partnership with: Deutsche Physikalische Gesellschaft and the Institute of Physics

OPEN ACCESS

RECEIVED
13 May 2020

REVISED
18 January 2021

ACCEPTED FOR PUBLICATION
21 January 2021

PUBLISHED
11 February 2021

PAPER

Ultrathin Co films with Pt and Au covers—magnetic and structural properties driven by Ga^+ ion irradiation

P Mazalski[1,2,*], L Ohnoutek[3], I Sveklo[2,*], L Beran[3], Z Kurant[2], W Powroźnik[4], A Wawro[5], M O Liedke[6], M Butterling[6], A Wagner[6], J Fassbender[7], J Hamrle[3], R Antoš[3], V Kletecka[3], M Veis[3,*] and A Maziewski[2]

[1] Jerzy Haber Institute of Catalysis and Surface Chemistry of the Polish Academy of Sciences, Cracow, Poland
[2] Faculty of Physics, University of Bialystok, Bialystok, Poland
[3] Faculty of Mathematics and Physics, Charles University in Prague, Prague 2, Czech Republic
[4] AGH University of Science and Technology, Department of Electronics, Cracow, Poland
[5] Institute of Physics Polish Academy of Sciences, Warsaw, Poland
[6] Institute of Radiation Physics Helmholtz-Zentrum Dresden-Rossendorf, Dresden, Germany
[7] Institute of Ion Beam Physics and Materials Research Helmholtz-Zentrum Dresden-Rossendorf, Dresden, Germany
[*] Authors to whom any correspondence should be addressed.

E-mail: jo@uwb.edu.pl, piotrmaz@uwb.edu.pl and veis@karlov.mff.cuni.cz

Keywords: perpendicular magnetic anisotropy, ion irradiation, structural properties, positron annihilation spectroscopy, molecular beam epitaxy, immiscible/miscible interfaces, magneto-optical Kerr spectroscopy

Supplementary material for this article is available online

Abstract

The X/Co 3 nm/Y (where X, Y = Au, Pt) trilayers with as deposited in-plane magnetization alignment were irradiated with 30 keV Ga^+ ions in the wide range of ion fluence. The samples were investigated by means of complementary techniques: magneto-optical magnetometry and spectroscopy (in the photon energy range from 1.2 eV to 4.5 eV), magnetic force microscopy, positron annihilation spectroscopy, x-ray diffraction and reflectivity. Difference in miscibility of interface atoms is clearly manifested in various intermixing extent at Co/Pt and Co/Au interfaces and consequently in magnetic properties of the irradiated trilayers. Low irradiation fluence ($\sim 10^{14}$ ions cm^{-2}) leads to $\sim$1 nm interfaces broadening without visible surface etching for all samples, which is related with a distinct drop of magnetic anisotropy. However, the high irradiation fluence ($\sim 5 \times 10^{15}$ ions cm^{-2}) results in enhanced interface broadening and significant surface etching ($\sim$5 nm) partially removing also Co atoms. Tensile strains (up to 0.5%) were developed in the cover layers. The tensile strain, layers intermixing and the creation of Co–Pt(Au) alloys with different composition formed by irradiation are correlated with the increase of magnetic anisotropy. Moreover it was observed that substitution of Au instead of Pt (as a cap or buffer layer) results in substantial increase of perpendicular magnetic anisotropy. Maximal increase of magnetooptical parameters was observed for Pt/Co/Pt layer. Irradiation induced changes of concentration profiles are revealed using magnetooptical spectra, x-ray reflectivity spectra and simulations with use of binary collision approximation.

1. Introduction

Ultrathin film systems containing a magnetic material such as Co, sandwiched between nonmagnetic metals, with tunable magnetic anisotropy are of particular importance for spintronic applications. The effective magnetic anisotropy of such structures is a result of the interplay between magnetocrystalline, magnetoelastic, surface (interface), and shape anisotropy contributions [1]. The Pt/Co is one of the most intensively studied systems due to its numerous applications [2]. Special attention was paid to the modifications of perpendicular magnetic anisotropy (PMA) of Pt/Co films obtained by thermal treatment [3–6], irradiation with ions [7–13] or light [14–16], due to the interface intermixing and the appearance of

the residual strains. Binary Co–Pt system is fully miscible forming a number of stable and metastable ordered alloys [17]. Some of them like tetragonal CoPt $L1_0$ or hexagonal Co_3Pt $D0_{19}$ phases exhibit strong magnetocrystalline anisotropy [18]. Ordering kinetics in Pt–Co bulk systems is relatively slow and requires sample heating to high temperature [19], but the interdiffusion increases significantly with the presence of large number of defects and intrinsic strains [20] and can occur at lower temperatures. In Al_2O_3/Mo/Pt/Co/Pt the Ga^+ irradiation enhances the intermixing of Pt and Co atoms at Pt–Co and Co–Pt interfaces and results in formation of alloys [21, 22]. Mixing at the interfaces (and Co–Pt alloying) is increased with irradiation fluences F. Observed changes in XMCD spectra after 30 keV Ga^+ irradiation were interpreted as an appearance of the partially ordered $L1_0$ CoPt phase [8]. A deeper insight into the origin of ion irradiation induced PMA requires relative comparison of structural changes after replacement of Pt covers with other metals such as Au. Due to Co–Au immiscibility this interface exhibits different from Co/Pt intermixing extent under ion irradiation [23]. The magnetic properties of ion irradiated ultrathin cobalt trilayers depend on various parameters such as: (i) Co layer thickness d_{Co} in Pt/Co/Pt [8]; (ii) type, fluence and energy of ions in Pt/Co/Pt [9, 13], (iii) thickness of the cover layers in Pt/Co/Pt [9]. Moreover, only limited studies of magnetooptical and XAS, XMCD studies were carried out on irradiated Co with Pt and Au covers [11, 23].

The goal of the present work is to perform combined studies of the irradiation induced modifications of magnetic and structural properties of ultrathin Co layers with different combinations of miscible (Pt) and immiscible (Au) covers using complementary experimental techniques. In our earlier works we considered ion irradiated stacks as built of effective components described by mean parameters. However, in more realistic considerations the in-depth structure is much more complex. In this work we take into account such structural complexity and model experimentally recorded properties with help of magnetooptical spectroscopy simulations. In comparison to our previous works [8, 13] magnetic anisotropy was also determined for both negative and positive magnetic anisotropy fields H_{1EFF}. Moreover, combined studies allow determination of PMA relation with irradiation induced tensile strains and irradiation driven changes in atom distribution for all of the ultrathin films.

On the basis of our earlier investigations of the wedge-shaped Co layers [8, 23], in which magnetic properties were determined as a function of both Co thickness and ion fluence of 30 keV Ga^+ irradiation, in the present work the thickness of the cobalt layer was selected slightly above the spin reorientation thickness. In such case the non-irradiated samples have in-plane magnetization and the value of magnetic anisotropy under ion irradiation can be significantly increased up to out-of-plane state. Mean penetration depth of Ga^+ ions with chosen energy of 30 keV is above a sum of thicknesses of cobalt and capping layers.

The structure of this paper is as follows. Experimental techniques including sample preparation are presented in section 2. The experimental results are reported in section 3, which is divided into three subsections corresponding to different measurement techniques. Results from polar Kerr magneto-optical effect (PMOKE) magnetometry, sensitive to the out-of-plane magnetization component, and magnetic force microscopy investigations of the domain structure are presented in subsection 3.1. The results of symmetric and asymmetric analysis of high angle x-ray diffraction and reflectivity measurements were presented in subsection 3.2. The results of magneto-optical spectroscopy measurements (Kerr rotation and ellipticity considered as a function of wavelength) of the samples subjected to irradiation with selected fluences are reported in subsection 3.3. Obtained dependences were fitted with help of multilayer model allowing to reveal cobalt concentration profile and compared with binary collision approximation model. In subsection 3.4 the results of positron annihilation spectroscopy, sensitive to vacancies which are generated in irradiation processes, are discussed. Detailed information on x-ray diffraction and reflectometry data are presented in the supplementary material (https://stacks.iop.org/NJP/23/023015/mmedia) section S1. In supplementary material section S2 the additional results of positron annihilation spectroscopy are given. Conclusions are presented in section 4.

2. Methods

Investigated series of Pt(Au) (20 nm, bottom)/Co (3 nm)/Pt(Au) (5 nm, top) trilayers were grown at room temperature by the molecular beam epitaxy on 10×10 mm^2 (0001) sapphire single crystal substrates. In the case of Au bottom layer preliminary 20 nm Pt buffer layer was deposited. From twelve-fold symmetry observed in XRD φ-scan measured for buffer Pt(220) and Au(220) reflections in relation to the positions of (11–20) Al_2O_3 substrate reflections one can conclude that two epitaxial relations between orientation substrate/buffer occurs: (i) Pt[111]||$A1_2O_3$[0001], Pt(110)||$A1_2O_3$(10–10), which is typical for high temperature growth Pt on (0001)Al_2O_3 [24] and (ii) Pt[111]||$A1_2O_3$[0001], Pt(110) ||$A1_2O_3$(11–20). Orientation of Au buffer is the same as of the Pt buffer. This co-existence of two possible orientation

relationships was already reported for Pt growth on MgO(001) substrate [25]. Nominal Co layer thickness of 3 nm was selected to achieve the in-plane magnetization orientation for as deposited films [23].

After deposition, each sample series was irradiated with a conventional ion implanter using 30 keV Ga^+ ions in the form of adjacent stripes (each 0.9 mm wide) with 20 monotonically grown fluences in the range of 0–1 $\times$ 10^{16} ions cm^{-2}. For structural measurements the samples (3 $\times$ 3 mm^2) were homogeneously irradiated with two selected fluences (1) 2.8 $\times$ 10^{14} and (2) 5 $\times$ 10^{15} ions cm^{-2}. The results obtained for Au/Co/Au sample irradiated with high fluence range (1 $\times$ 10^{15}–1 $\times$ 10^{16} ions cm^{-2}) due to degradation of magnetic properties during aging are excluded from consideration.

X-ray structural measurements were done with Philips X'pert four axis diffractometer equipped with optics suitable for epitaxial thin film analysis at the Cu $K_{\alpha 1}$ wavelength of 1.540 59 A.

The measurements of Doppler broadening of the annihilation line by variable energy positron annihilation spectroscopy (DB-VEPAS) as well as coincidence Doppler broadening (cDB) at fixed positron implantation energy of $E_p = 3$ keV have been carried out using the apparatus for *in-situ* defect analysis [26] at the slow positron beamline SPONSOR [27]. By using slow positron accelerators which produce monokinetic positrons beams with energy varying from 0.05 to 35 keV it is possible to study depth profiles of defects from the surface to about 1 μm (in the case of Pt film). Doppler broadening of the annihilation line was measured by single high-purity germanium (HPGe detector) with an energy resolution of 1.09 $\pm$ 0.01 keV at 511 keV. cDB, providing the analysis of elemental decoration of the positron annihilation site, was measured by using two HPGe detectors with energy resolution of 780 $\pm$ 20 eV at 511 keV.

PMOKE home-built microscopes equipped with a CCD camera and appropriate digital image processing software (in PMOKE configuration the measured signal intensity is proportional to the component of perpendicular magnetization) enabled: (i) recording the images of remanent magnetization distribution after saturation in out-of-plane direction; (ii) determination the local magnetization loops with a lateral resolution of 10 μm for entire sample surface (i.e. simultaneously for all irradiation fluences). PMOKE magnetometry measurements, as a function of perpendicular to sample applied magnetic field $H_\perp$, were performed at nearly normal light incidence, using laser beam with wavelength 635 nm (1.97 eV) focused to 0.3 mm spot.

Magneto-optical Kerr spectroscopy in the photon energy range from 1.2 eV to 4.5 eV using rotating analyzer was performed at the angle of incidence of 65° in the out-of-plane magnetic field of $\mu_0 H = 682$ mT high enough to saturate the sample magnetization. The sample was mounted at *XY* translation stage allowing to acquire the PMOKE spectra at the center of each stripe. High pressure Xe lamp was used as a light source and the light beam was focused on the sample by a set of lenses, resulting in the light spot considerably smaller than the stripe width. The light at the output of the apparatus was focused into an optical fiber and analyzed by an Andor Shamrock spectrometer.

A 4 $\times$ 4 transfer matrix formalism for anisotropic media [28] was used to calculate the magneto-optical response for different concentration profile models. The calculations were performed for profiles consisting of plane parallel layers with different thicknesses. Magneto-optical properties of Co_xPt_{1-x} alloys are changed significantly with concentration x and can be therefore exploited for the evaluation of the alloying at interfaces as a function of fluence [29–31]. The optical parameters (diagonal elements of permittivity tensor) of Au, Co and Pt were taken from literature [32, 33]. Spectroscopic ellipsometry measurements were carried out on bare Al_2O_3(0001) substrate and the experimental ellipsometric angles were fitted using Cauchy relation to obtain its optical parameters. The magneto-optical parameters (non-diagonal elements of permittivity tensor) of Co were taken from reference [30]. In the case of the samples where the Co layer was grown on Pt buffer, the optical and magneto-optical parameters were obtained from ellipsometric and magneto-optical measurements on non-irradiated sample. This sample was grown using the same deposition conditions in different runs, however slightly differs in Co thickness ($d_{Co} = 3.3$ nm, $d_{Pt} = 5$ nm). The results of x-ray reflectivity (XRR) fits were used to determine the layer thicknesses and surface roughness as the knowledge of these variables was necessary to calculate the optical and magneto-optical parameters of Co. The depth profile of Co and Pt concentration at the interfaces was approximated by a step-wise profile. The set of Co_xPt_{1-x} alloys with discrete concentration $x = 0.28$, 0.47, 0.59, 0.72 were used for profile approximation in irradiated samples. Their optical parameters were calculated using effective medium approximation (EMA) [34] taking into account the optical constants of Co [33] and Pt [32]. Their magneto-optical parameters were calculated using the experimental results published in references [29, 30]. Similarly, for the Co and Au layers, the intermixing of their interfaces was approximated by steps in concentration profiles. Due to the immiscibility of Co and Au, it was assumed that Co forms nanoparticles dispersed in Au matrix. Both the optical and the magneto-optical parameters of such structure were calculated by EMA [34, 35]. A set of Co_yAu_{1-y} layers with $y = 0.2$, 0.4, 0.6, 0.8 was used for interface approximation and the calculations of the PMOKE spectra. The depth concentration profiles for different irradiation fluences are determined from the best agreement between the calculation model

and the experimental PMOKE spectra.

To observe magnetic domain structure in submicrometer range magnetic force microscopy (MFM) measurements were done with a commercial (NT-MDT) setup operating in tapping mode at ambient conditions equipped with low moment magnetic cantilevers MESP-LM (Bruker). Before the MFM measurements, the samples were demagnetized in a decaying ac magnetic field oriented perpendicularly to the surface.

3. Results

3.1. PMOKE magnetometry and MFM imaging of domain structure

The cross-section scheme of the four studied sample structures, lateral fluence distribution and resulting PMOKE remanence image obtained after irradiation are shown in figures 1(a)–(d)). Within each sample the PMOKE images show stripe-like structure related to the applied Ga^+ ion fluence F. The gray scale illustrates magnetization remanence state—brighter stripes correspond to larger magnetization component in perpendicular direction. PMOKE ($H_\perp$) hysteresis loops for selected fluences marked as 1–3 are shown at the bottom.

In the as-deposited trilayers ($F = 0$ ions cm^{-2}) the magnetization is aligned in the sample plane and appropriate PMOKE hysteresis loops have the shape reflecting magnetization rotation from in-plane to out-of-plane state. In the remanence image for Pt/Co/Pt sample (figure 1(a)) two bright regions are clearly visible, i.e. two fluence regions with PMA and remanence magnetization exhibits out-of-plane component. These two areas with enhanced remanence correspond to branch 1 (low fluence) and branch 2 (high fluence), respectively, as previously reported in reference [8]. Thus, for Pt/Co/Pt sample the maximum of remanence in branch 1 is occurred at fluence of 2×10^{14} ions cm^{-2}, whereas in branch 2 at 4×10^{14} ions cm^{-2}. The enhancement of remanence is clearly visible in appropriate PMOKE hysteresis loops for fluences 1 and 2 at the bottom. Different magnetization modification takes place after the replacement of the Pt capping layer with Au (Pt/Co/Au sample)—only one region with enhanced out-of-plane magnetization (up to PMA) can be obtained (figure 1(b)). For smaller ion fluences only minor increase in anisotropy fields were observed. In the case of Au/Co/Pt sample (figure 1(c)) the magnetization modification is more similar to that observed for Pt/Co/Pt but the value of enhanced out-of-plane magnetization is slightly smaller. However, no enhanced out-of-plane magnetization was detected in Au/Co/Au system (figure 1(d)). All studied systems subjected to ion fluences higher than $>8 \times 10^{15}$ ions cm^{-2} exhibit a superparamagnetic behavior.

For each irradiated stripe (with defined fluence) the following magnetic and magneto-optical parameters describing PMOKE hysteresis loop were determined: (i) the maximum PMOKE rotation, θ_{MAX}; (ii) the remanent PMOKE rotation, θ_{REM}, (iii) coercivity H_C, and (iv) saturation field H_{SAT}. The saturation field was used to determine magnetic anisotropy field $H_{1EFF} = 2K_{1EFF}/\mu_0 M_s$, (where K_{1EFF} and M_S are the effective uniaxial anisotropy constant and saturation magnetization respectively) as $H_{SAT} = H_{1EFF}$ in the region of in-plane magnetization state—characterized by non-hysteretic curves. In the region of out-of-plane magnetization state H_{1EFF} was determined analyzing magnetization curves registered with both in-plane and out-of-plane magnetic fields providing single domain state. These curves were fitted in Stoner–Wohlfarth model approximation. Figure 2 depicts θ_{MAX}, θ_{REM}, H_C and H_{1EFF} dependences on the fluence.

For three of the studied systems, except Au/Co/Au, one can find that with fluence F increase the maximum PMOKE rotation θ_{MAX} has one peak (see figures 2(a)–(c)) with increase of 2.3, 1.5, 1.6 times compared to non-irradiated state for Pt/Co/Pt, Pt/Co/Au and Au/Co/Pt, respectively. Such increase in θ_{MAX} is correlated with Co–Pt alloy formation [36, 37] as a function of the ion fluence. More detail discussion of this effect is provided in subsection 3.2. For fluences $F > 1 \times 10^{15}$ ions cm^{-2} a subsequent decrease in θ_{max} is a result of the sample sputtering including also magnetic material. In the case of Au/Co/Au/ system the magneto-optical response is practically unnoticeable for low fluence region (figure 2(d)).

Drop in magnetic anisotropy field H_{1EFF} at low fluence range ($\sim 10^{13}$ ions cm^{-2}) is visible for all cover combinations and can be explained as a partial decrease of surface anisotropy due to interface mixing [8], which is studied earlier for irradiation of thinner cobalt samples with PMA state [37]. For larger fluences we observed in all studied systems non-monotonic growth of magnetic anisotropy fields with two maxima: first, called as branch 1, appears for the fluence $\sim 2 \times 10^{14}$ ions cm^{-2} and second, branch 2, less distinct, is visible for fluences $>2 \times 10^{15}$ ions cm^{-2}. Their relative amplitudes depend on the type of covers. In Pt/Co/Pt and Au/Co/Pt systems H_{1EFF} takes a value close to zero (see figures 2(a) and (c)) for both branches, but for Au/Co/Pt only in the second branch the H_{1EFF} is getting positive—characteristic feature of

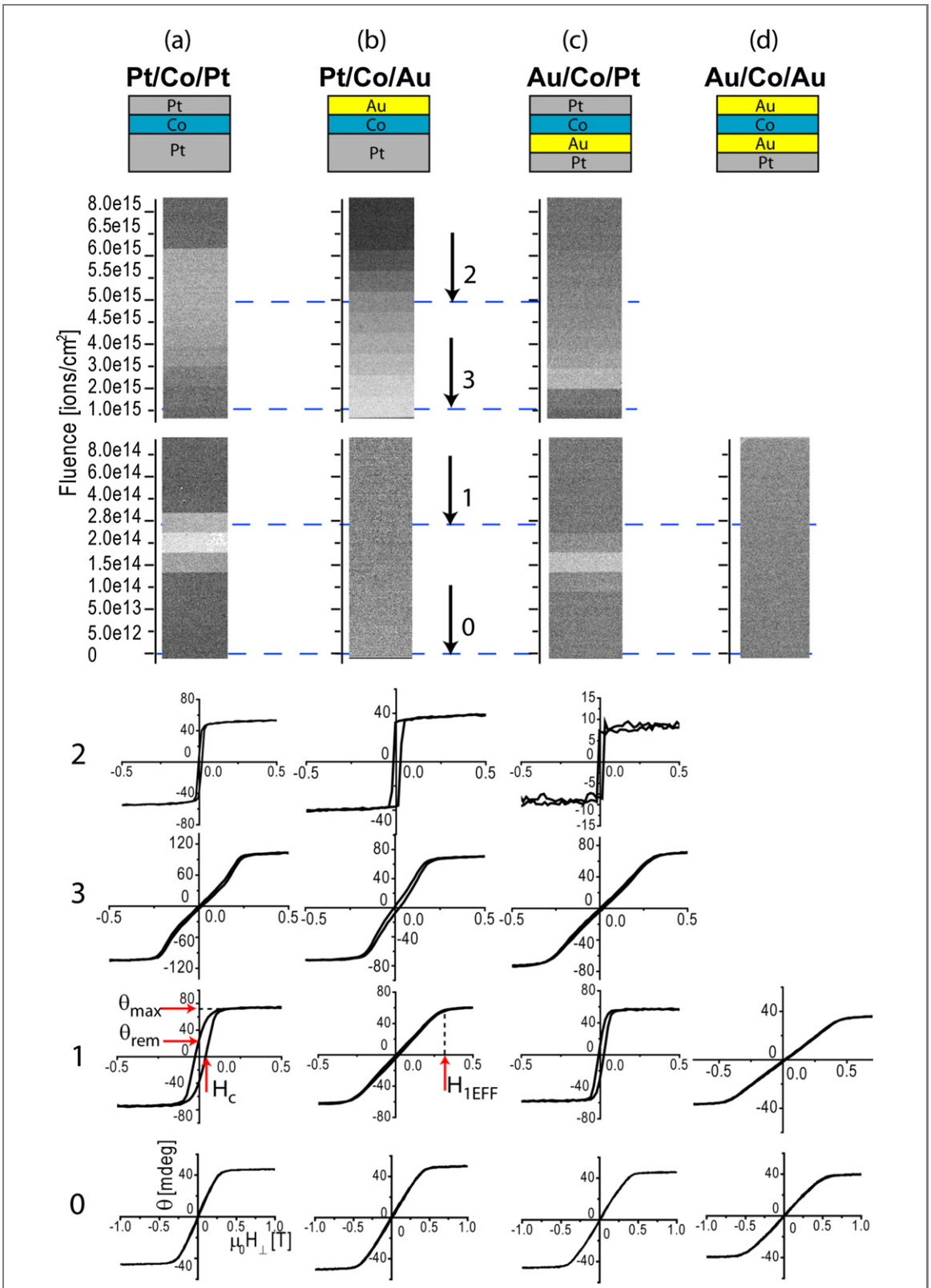

Figure 1. Gray scale PMOKE remanence images of the studied samples: (a) Al_2O_3/Pt/Co/Pt, (b) Al_2O_3/Pt/Co/Au, (c) Al_2O_3/Pt/Au/Co/Pt, (d) Al_2O_3/Pt/Au/Co/Au. Out-of-plane component of local magnetization is proportional to the intensity of gray scale remanence images, while zero remanence corresponds to black. The exemplary PMOKE hysteresis loops are shown at the bottom in appropriate columns. The numbers 1–3 correspond to fluences 1–3 marked with arrows in remanence images: 1 corresponds to fluence at branch 1, 2—branch 2, and 3—transient fluence between branch 1 and 2; 0 corresponds to non-irradiated samples. Fluences 1 and 2 were selected for uniform irradiation of the samples for structural studies. The definitions of characteristic parameters: maximal Kerr rotation θ_{MAX}, remanence θ_{REM}, magnetic anisotropy field H_{1EFF} ($=H_{SAT}$) for the samples with in-plane magnetization are schematically shown.

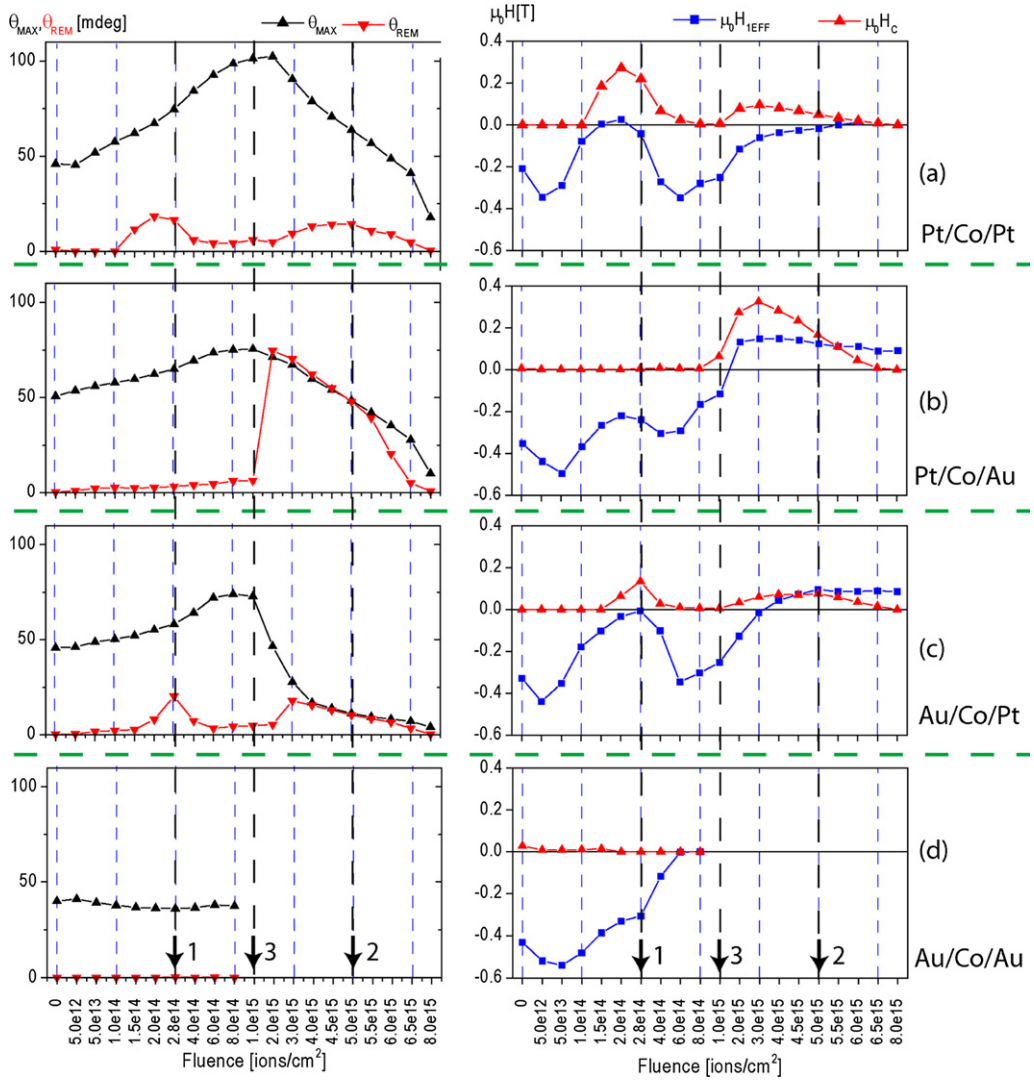

Figure 2. The magnetic parameters for different samples are presented in four rows: (a) Pt/Co/Pt, (b) Pt/Co/Au, (c) Au/Co/Pt, (d) Au/Co/Au. Fluence dependences of: (first column) Kerr rotation: maximal θ_{MAX} (black triangles up), at remanence θ_{REM} (red triangles down), (second column) magnetic anisotropy H_{1EFF} (blue squares) and coercivity H_C (red triangles up). Kerr rotation parameters were derived from the appropriate PMOKE hysteresis loops. The arrows 1–3 indicate the fluences as in figure 1. The lines, connected experimental points, are drawn as guides to the eye.

a system with PMA. At the branch 1 the Pt/Co/Au/ and Au/Co/Au/ systems exhibit negative values of H_{1EFF} which indicates enhanced remanence magnetization only. Presented dependencies indicate the importance of Pt layer in PMA enhancement after irradiation. The appearance of the branch 1 could be explained by induced tensile strains [10] which are expected for all discussed Co covers and possible creation of Co–Pt alloys [8]. Co-platelets seem to be responsible for branch 2 creation [38]. Taking into account initial values of H_{1EFF} for pristine samples, one can evaluate the maximal increase of anisotropy fields after irradiation as 0.3÷0.4 T. It is interesting, that the lowest value of this increase is observed in Pt/Co/Pt system. Therefore, it seems that Au as a cover layer supports creation of anisotropic Co-platelets in branch 2. Fluence dependence of coercivity field H_C, determined from PMOKE curves analysis, is plotted in the second column of figure 2. Noticeable values of H_C were recorded for fluences corresponding to branch 1 or 2 with nonzero remanence—cf θ_{REM} and H_C dependences in figure 2.

To underline the difference in magnetic anisotropy induced by ion irradiation in the studied systems a comparison data are presented in table 1. Observed significant changes between studied systems are described quantitatively by the following parameters: (i) $\Delta H_{b1} = H_{1EFF}(\text{branch 1}) - H_{1EFF}(F = 0)$, (ii) $\Delta H_{b2} = H_{1EFF}(\text{branch 2}) - H_{1EFF}(F = 0)$, where H_{1EFF}(branch 1 or branch 2) is the effective anisotropy field of the samples irradiated with fluences corresponding to branch 1 or 2, $H_{1EFF}(F = 0)$ is the effective anisotropy field of the as deposited sample. It is visible that substitution of Au instead of Pt as a buffer layer induces higher changes of magnetic anisotropy especially for higher ion irradiation fluence. Au as a capping layer significantly increase magnetic anisotropy field for branch 2 fluence.

Table 1. Magnetic anisotropy fields and their changes after irradiation with branch 1, 2 fluences. Definitions of listed parameters are provided in the text.

	Pt/Co/Pt	Pt/Co/Au	Au/Co/Pt	Au/Co/Au
$H_{1\text{eff}}$ $(F=0)$ (T)	−0.21	−0.35	−0.32	−0.42
ΔH_{b1} (T)	0.24	0.14	0.3	0.1
ΔH_{b2} (T)	0.18	0.5	0.43	

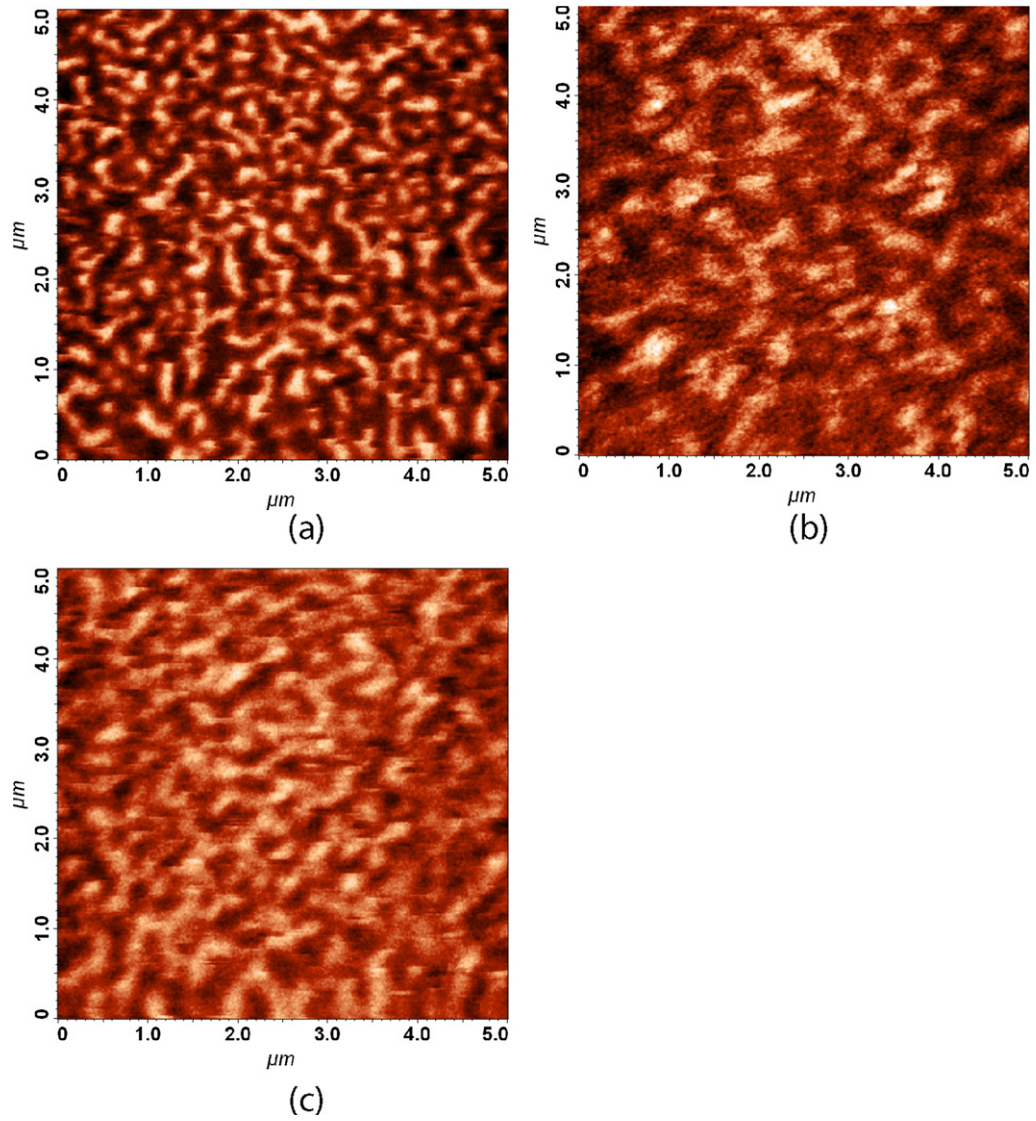

Figure 3. MFM images of domain structure: (a) Pt/Co/Pt, fluence 2×10^{14} ions cm^{-2} (corresponds to branch 1 in figure 2(a)); (b) Pt/Co/Au, fluence 3×10^{15} ions cm^{-2} (branch 2 in figure 2(b)); (c) Au/Co/Pt, fluence 2.8×10^{14} ions cm^{-2} (branch 1 in figure 2(c)).

Domain structures with out-of-plane magnetization are expected in areas with a fluence creating PMA state. Because of lateral resolution limit, it was not possible to visualize these domains using PMOKE microscope, as domains with submicrometer sizes are expected. Their observation demand application high resolution domain imaging techniques, e.g. MFM. Before imaging the samples were demagnetized in ac-decaying normal field. Submicrometer domain structures images registered with use of MFM for Pt/Co/Pt, Pt/Co/Au/ and Au/Co/Pt samples are presented for the fluences appropriate to PMA state (figures 3(a)–(c)). Visible structures are not regular. Gaussian fits to the peak of the radially averaged intensity of the Fourier transforms give central periods of 0.5, 0.8, and 0.7 μm, respectively.

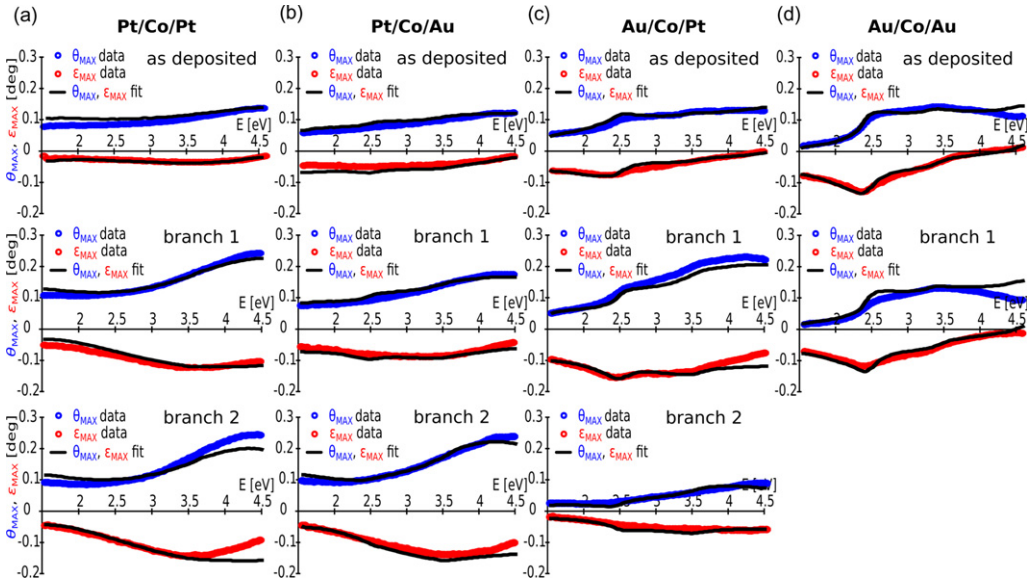

Figure 4. Experimental (thick blue and red lines) and calculated (thin black lines) magnetooptical complex polar Kerr spectra obtained for four systems at branch 1 and 2 fluences: (a) Pt/Co/Pt, (b) Pt/Co/Au/, (c) Au/Co/Pt/ and (d) Au/Co/Au.

3.2. Magneto-optical spectroscopy

In order to describe changes at magnetic interfaces after the irradiation process and creation of various Co_xPt_{1-x} alloys, which are responsible for observed magneto-optical (MO) and magnetic changes, the MO spectroscopy studies were performed. This approach combines experimental observations of wavelength dependent Kerr MO effect with advanced theoretical modeling including both layers thicknesses and Co_xPt_{1-x} compositions. Figures 4(a)–(d)) present the measured MO spectra for all studied systems at three fluence regions of interest—as deposited and irradiated with fluences corresponding to the maximal changes of the saturation field (branch 1 and 2). Theoretically calculated spectra being the best fits to the experiment data are shown in figure 4 as well. The fits were calculated varying thicknesses of individual sublayers, as well as EMA contribution (depending on the system composition). The resulting values of the applied parameters are listed in table 2. The calculated depth profiles of Co concentration are shown in figures 5(a)–(d)) for all branches of the samples to illustrate the intermixing after irradiation. The step-like Co profiles describe sub-layers of different alloys Co_xPt_{1-x} and/or Co_yAu_{1-y} EMA contribution based on the data presented in table 2. Cobalt concentration depth profiles obtained after fitting the MO spectra are shown together with the Co profiles obtained from XRR and TRIDYN simulations [39].

For as-deposited (non-irradiated) trilayers, the thicknesses of Co layer according to the theoretical calculations of MO spectra are in reasonable agreement with sample deposition protocols and XRR data (figure 5, upper row). The blurring of Co interfaces in XRR profiles are ascribed to the natural waviness of interfaces visible as interdiffusion at small sliding angles used in this method. Small systematic depth shift can be explained by low sensitivity of MO to the total film thickness when it exceeds extinction length—in Pt the extinction length is 25 nm for $\lambda = 640$ nm. The biggest discrepancies between theoretical and measured MO spectra are observed for Pt/Co/Pt system in the θ_{MAX} spectrum (figure 4(a)). This difference between the model and the experiment in the lower photon energy region may origin in slightly different optical properties of Co or Pt layers from tabulated values. This can be the result of different bulk density (and consequently free carriers concentration) of the layers due to differences in preparation procedure (and resulting crystallinity), which usually manifests itself in the low energy spectral region via Drude dispersion [40]. Moreover, the proposed theoretical model structure suggests a presence of Co–Pt alloy at all Co–Pt interfaces in non-irradiated samples, but no Au–Co alloy at all. This agrees with previously published results [41, 42] and clearly demonstrates a strong tendency of Co and Pt to create the alloy or rough Co–Pt interface. On the contrary, the Au–Co alloying does not occur in non-irradiated samples. Although the model structure of Pt/Co/Au and Au/Co/Pt systems considers the same amount of alloying, the agreement between theoretical fit and experimental data is clearly better in the case of Au/Co/Pt system. This suggests that the bottom Co interface with Au layer is of higher quality in contrast than with Pt layer since the model considers perfectly abrupt interfaces. The perfect description of experimental data by theoretical model in non-irradiated Au/Co/Au sample clearly demonstrates the highest quality of interfaces in this sample. A good agreement between experimental data and the model considering nominal sample

Table 2. Distribution of Co, Pt, Au along the multilayer depth in four Pt(Au)/Co/Pt(Au) systems for as deposited structures and selected ion irradiation fluences corresponding to branch 1 and 2, determined from the best fit to the magneto-optic complex polar Kerr effect spectra.

	As deposited				Branch 1				Branch 2		
Component	Pt/Co/Pt	Pt/Co/Au	Au/Co/Pt	Au/Co/Au	Pt/Co/Pt	Pt/Co/Au	Au/Co/Pt	Au/Co/Au	Pt/Co/Pt	Pt/Co/Au	Au/Co/Pt
	Layers thickness (nm)				Layers thickness (nm)				Layers thickness (nm)		
(top) Pt	4.80	0.00	4.80	0.00	3.16	0.00	2.83	0.00	0.00	0.00	0.00
Au	0.00	5.00	0.00	5.00	0.00	2.26	0.00	1.80	0.00	0.00	0.00
CoPt alloy (72%Pt)	0.15	0.00	0.15	0.00	1.40	0.00	1.70	0.00	0.00	0.00	0.00
EMA 80% Au, 20% Co	0.00	0.00	0.00	0.00	0.00	1.50	0.00	2.00	0.00	0.00	0.00
CoPt alloy (53%Pt)	0.10	0.00	0.10	0.00	1.15	0.00	1.40	0.00	0.00	0.00	0.00
EMA 60% Au, 40% Co	0.00	0.00	0.00	0.00	0.00	1.00	0.00	1.00	0.00	0.00	0.00
CoPt alloy (41%Pt)	0.05	0.00	0.05	0.00	0.40	0.00	0.35	0.00	0.00	0.00	0.00
EMA 40% Au, 60% Co	0.00	0.00	0.00	0.00	0.00	0.80	0.00	0.50	0.00	0.00	0.00
CoPt alloy (28%Pt)	0.05	0.00	0.05	0.00	0.20	0.00	0.20	0.00	0.00	0.00	0.00
EMA 20% Au, 80% Co	0.00	0.00	0.00	0.00	0.00	0.60	0.00	0.50	0.00	0.00	0.00
Co	2.69	2.85	2.85	3.00	0.39	0.00	0.00	0.00	0.00	0.00	0.00
CoPt alloy (28%Pt)	0.05	0.05	0.00	0.00	0.20	0.20	0.00	0.00	0.00	0.00	0.00
EMA 20% Au, 80% Co	0.00	0.00	0.00	0.00	0.00	0.00	0.05	0.50	0.00	0.00	0.00
CoPt alloy (41%Pt)	0.05	0.05	0.00	0.00	0.40	0.40	0.00	0.00	0.00	0.00	0.00
EMA 40% Au, 60% Co	0.00	0.00	0.00	0.00	0.00	0.00	0.05	0.50	0.00	0.00	0.00
CoPt alloy (53%Pt)	0.10	0.10	0.00	0.00	1.15	1.15	0.00	0.00	1.00	0.00	1.25
EMA 60% Au, 40% Co	0.00	0.00	0.00	0.00	0.00	0.00	1.00	1.00	0.00	0.00	3.75
CoPt alloy (72%Pt)	0.15	0.15	0.00	0.00	1.40	1.40	0.00	0.00	3.50	8.00	0.00
EMA 80% Au, 20% Co	0.0	0.00	0.00	0.00	0.00	0.00	2.00	2.00	0.00	0.00	0.00
Au	0.00	0.00	20.00	20.00	0.00	0.00	17.50	20.00	0.00	0.00	15.00
Pt (bottom)	19.80	19.80	20.00	20.00	18.16	18.16	20.00	17.50	16.95	14.00	20.00

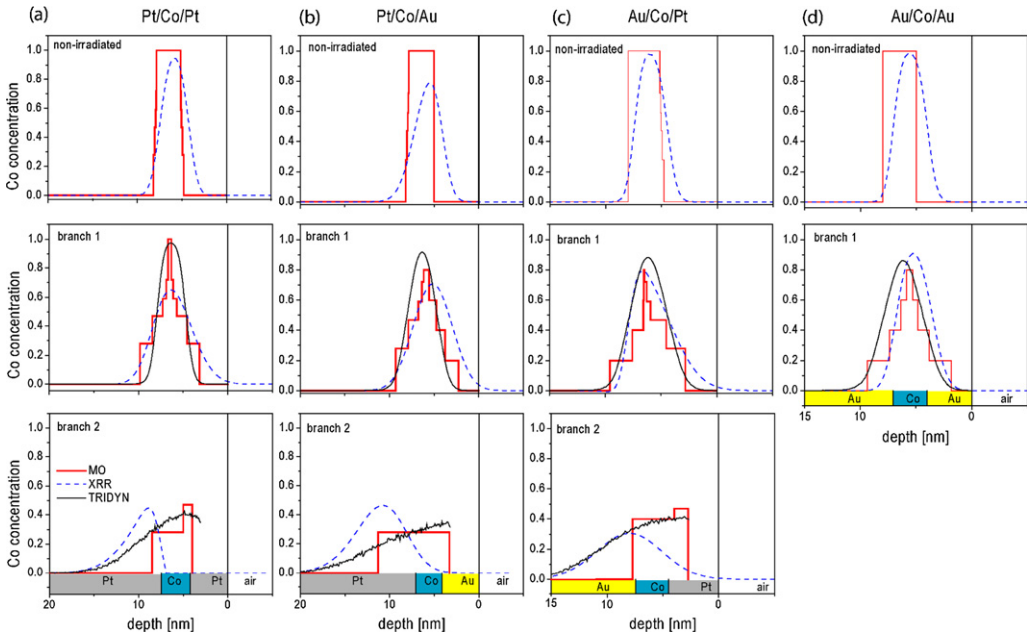

Figure 5. The depth profiles of Co concentration in (a) Pt/Co/Pt, (b) Pt/Co/Au/, (c) Au/Co/Pt/, (d) Au/Co/Au samples calculated as: the best fit step-like function to the experimentally obtained MO spectra (red line), XRR fitting (dashed blue line), and TRIDYN simulations (black line). Top row corresponds to non-irradiated samples, middle—irradiated with branch 1 fluence, and bottom—with branch 2 fluence. Non-irradiated sample structures obtained from XRR fits are schematically shown at the bottom.

structure has not been achieved for Pt/Co/Pt system [41, 42]. A slight discrepancy between 2.5–3 eV is probably due to a deviation of optical properties of Au from tabulated values. In this spectral region the Au exhibits sharp absorption bands whose energy strongly depends on crystallinity of the material [43].

The amplitudes of θ_{MAX}, ε_{MAX} spectra, measured for the branch 1 samples, increase with respect to non-irradiated ones, except Au/Co/Au system. This is connected with ion induced mixing of the layers which increases total volume of CoPt alloy in the sample. Depending on the composition, CoPt alloy can significantly enhance the PMOKE amplitude [18, 36, 44], influenced by the coupled 3d levels of Co and 5d

levels of Pt (with high spin–orbit interaction) [45]. Measured spectra are also consistent with those obtained from PMOKE θ_{MAX} measurements at wavelength $\lambda = 640$ nm presented in figure 2. The magneto-optical models are in a good agreement with experimental data and confirm significant intermixing of the Co and Pt layers, which corroborate quite well Co distribution obtained from the XRR and TRIDYN calculations (figure 5). These results suggest that nearly no pure Co remains in the stripe (or this effect is due to the significant Co–Pt, Au roughness). Etching of the Pt or Au capping layer for these fluences is negligible. TRIDYN calculations give symmetric mixing of both Co interfaces even for asymmetric covers, which is explained by disregarding of chemical driving forces in the model of binary collision approximation. Comparison of the MO model structures for asymmetric Pt/Co/Au and Au/Co/Pt systems shows that after irradiation the spread of Co across Au cover is different than in Pt one. These results can be explained by different behavior of Pt and Au during irradiation. While Pt tends to form a miscible alloy with Co, Au is immiscible and intermixing of Co and Au is suppressed by thermal spikes and temperature segregation processes [46] leading to discontinuity of the Co layer. An increased discrepancy between experimental data and theoretical model is visible for Au/Co/Au system (figure 4(d), branch 1). Similar disagreement can be observed at the same photon energies for Pt/Co/Au system (figure 4(c), branch 1). This can be a result of the change of optical properties of bottom Au cover due to Ga^+ ion implantation inside it, since the d-bands of Au are located in this energy range.

When the samples were irradiated with branch 2 fluences the top layer containing intermixed cobalt becomes to be etched by Ga^+ ions. Thus, while the etching decreases the volume of magnetic material inside the sample, the resulting MO spectra of Au/Co/Pt system measured at branch 2 exhibit a lower amplitude than at branch 1. On the other hand, Pt/Co/Pt and Pt/Co/Au systems exhibit similar or higher amplitude. This can be explained by formation of magnetic Pt–Co alloy which increases the magneto-optical response with respect to pure Co. On the contrary, in Au/Co/Pt system the whole platinum layer is etched and only cobalt embedded into the Au layer is conserved. All changes in spectral amplitudes agree well with PMOKE hysteresis loops (figure 1). It should be noted, that calibration Pt–Co alloys used for MO spectra fittings were obtained in equilibrium conditions, which are different (and magneto-optical properties, too) for high fluence branch 2 irradiation mixing. For example, after high fluence irradiation the formation of metastable cobalt nano-platelets was reported in reference [38]. These differences can be responsible for the observed shift between lines determined from fitting by MO spectroscopy and XRR or TRIDYN simulations. In the case of Au/Co/Au branch 2 the MO signal was bellow detection limit of our spectrometer.

Although the theoretical calculations describe the experimental spectra in reasonable way, the noticeable deviations are observed, especially for branch 2. That might be connected with modification of magneto-optical properties due to severe structural disordering. Besides it, the EMA approximation assumed spherical Co nanoparticles dispersed in Au matrix, whereas in the real disordered material the shape of the nanoparticles should be irregular. Moreover, in the simulated structural models the samples are considered as the stacks of layers with ideally flat interfaces, while the interfaces in the real nanostructures are likely rough. These assumptions may not be fully valid in the case of branch 2 where the system of layers is not well defined.

3.3. XRR, symmetric and asymmetric XRD measurements

Detail structural analysis of as deposited samples and subjected to ion irradiation with fluences corresponding to branch 1 and 2 formation was carried out by means of XRR. Simulations were performed using PANanalytical commercial software based on the Parrat's formalisms (see figures S37–S48 in supplementary material). The scattering length density (SLD) profiles, used for the fittings, are shown in figure 6. Due to possible etching of irradiated samples, their SLD profiles were slightly shifted in depth to conserve the position of Al_2O_3 interface as in non-irradiated samples. SLD depth profiles of Co layers normalized on its bulk value were used as Co concentration profiles in figure 5. Taking into account from TRIDYN simulation that mean penetration depth for 30 keV Ga^+ ions is about 10 nm [47] and sputter yield for Au reaches 12.8 atoms/ion and for Pt 8.5 atoms/ion [48], the analysis of SLD profiles in figure 6 is the following.

All as prepared samples have flat interfaces roughnesses below 1 nm, and component layer thick nesses are close to nominal values. After irradiation corresponding to branch 1 layered structure of the samples is conserved in general and the sample surface (roughness of capping layer) is not changed. Irradiation-induced changes are visible for two upper layers—capping layer and Co layer below. The upper interface (closer to the sample surface) is mixed to a higher extent than the bottom one (far from the surface). Co–Pt interface is more spread than Co–Au due to different miscibility of Co–Pt (miscible) and Co–Au (immiscible) systems. The thickness of capping layer is slightly reduced by about 0.5–1 nm.

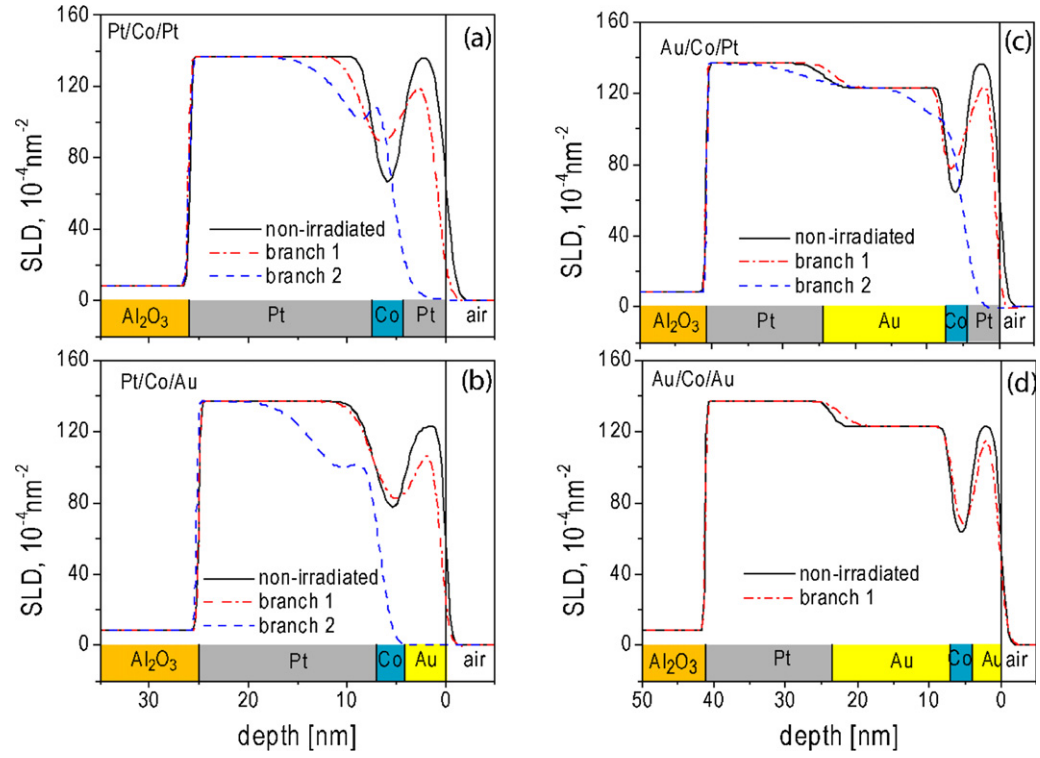

Figure 6. Depth profiles of electron SLD for non-irradiated and irradiated samples with fluences corresponding to branch 1 and 2: (a) Pt/Co/Pt; (b) Pt/Co/Au; (c) Au/Co/Pt and (d) Au/Co/Au. Non-irradiated sample structures obtained from XRR fits are schematically shown at the bottom.

After irradiation with branch 2 fluence, the capping layers are significantly ablated; the interfaces between the Co and capping/bottom layers are very smooth, thus the covering layers and Co are strongly intermixed.

In the high resolution θ–2θ x-ray diffraction spectrum the reflections from Pt(111), Au(111) and substrate Al_2O_3(0006) are clearly observed (see figures S1–S4 in supplementary material). Reflection Co(0002) is too weak and cannot be used for interplanar spacing calculation. Therefore we used Pt(111) and Au(111) reflections, assuming that after irradiation the change in lattice deformation is locally coherent and in consequence change the strain of neighbor layers is the same. For Pt/Co/Au film the intensity of Au(111) reflection is about 100 times weaker than Pt(111) reflection. This indicates that main contribution to the (111) reflection comes from the buffer layers. When the sample is tilted from normal measurement configuration at the angle $\psi = 35.26°$ it is possible to find asymmetric reflections from Pt(220) and Au(220) planes.

In biaxial strain model [49] it is assumed that layer exhibits in-plane ε_{xx} and out-of-plane ε_{zz} deformations connected via Poisson's ratio ν as $\frac{\varepsilon_{xx}}{\varepsilon_{zz}} = -\frac{1-\nu}{2\nu}$. According to this definition the deformations correspond to the appropriate interplanar distances as $\varepsilon_{xx} = \frac{d_x}{d_x^0} - 1$ and $\varepsilon_{zz} = \frac{d_z}{d_z^0} - 1$, where $d_x{}^0$ and $d_z{}^0$ are unstrained interplanar spacing related to the unstrained fcc lattice constant a_0 as $d_x^0 = d_{211}^0 = \frac{a_0}{\sqrt{6}}$, $d_z^0 = d_{a11}^0 = \frac{a_0}{\sqrt{3}}$. Direction $[-211]$ (x-direction) is perpendicular to the sample normal [111] (z-direction) and measured interplanar spacing (220) d_{022} can be decomposed into two perpendicular components as $\frac{1}{d_{022}^2} = \frac{16}{9} \cdot \frac{1}{d_{111}^2} + \frac{4}{9} \cdot \frac{1}{d_{211}^2}$. Using Poisson's ratio for Pt 0.36 and 0.4 for Au and measured interplanar spacing d_{022} and d_{111} one can determine in-plane interplanar spacing $d_x = d_{211}$, in-plane and out-of-plane strains ε_{xx} and ε_{zz} and unstrained lattice constant a_0. The summary of results is given in table 3.

In the case of Au/Co/Au and Au/Co/Pt samples 20 nm Pt buffer was used, so the Pt(111) reflection was occurred from this Pt buffer which is placed more deeper than ion penetration depth and consequently is not considered in irradiation process. Fluence dependences of derived lattice constant a_0 and in-plane stress are presented in figure 7. Analyzing the data it should be noted that for non-irradiated samples lattice constants a_0 are close to their bulk values—4.078 A for Au and 3.924 A for Pt. Irradiation with branch 1 fluence lead to low contraction about 0.1% which is further developed to 0.5% for branch 2 irradiation and can be ascribe to Ga^+ implantation.

Table 3. Measured interlayer spacing d_{111}, d_{220} and calculated in-plane interlayer spacing d_x, strains ε_{xx}, ε_{zz} and unstrained lattice constant a_0.

	Material	Pt			Au		
Sample	Fluence	0	Branch 1	Branch 2	0	Branch 1	Branch 2
Pt/Co/Pt	d_{111} (A)	2.264	2.259	2.248			
	d_{220} (A)	1.388	1.386	1.380			
	d_x (A)	1.607	1.607	1.601			
	a_0 (A)	3.929	3.925	3.907			
	ε_{xx} (%)	0.187	0.320	0.399			
	ε_{zz} (%)	−0.166	−0.284	−0.354			
Pt/Co/Au	d_{111} (A)	2.265	2.260	2.243			
	d_{220} (A)	1.388	1.386	1.379			
	d_x (A)	1.606	1.607	1.606			
	a_0 (A)	3.929	3.925	3.908			
	ε_{xx} (%)	0.149	0.307	0.647			
	ε_{zz} (%)	−0.132	−0.273	−0.575			
Au/Co/Pt	d_{111} (A)	2.267	2.267	2.272	2.352	2.345	2.329
	d_{220} (A)	1.389	1.388	1.390	1.443	1.441	1.430
	d_x (A)	1.607	1.603	1.601	1.674	1.674	1.660
	a_0 (A)	3.931	3.927	3.930	4.087	4.081	4.049
	ε_{xx} (%)	0.153	0.011	−0.174	0.337	0.499	0.415
	ε_{zz} (%)	−0.136	−0.010	0.154	−0.300	−0.443	−0.369
Au/Co/Au	d_{111} (A)	2.264	2.264		2.356	2.346	
	d_{220} (A)	1.388	1.388		1.444	1.440	
	d_x (A)	1.608	1.606		1.670	1.672	
	a_0 (A)	3.930	3.927		4.085	4.079	
	ε_{xx} (%)	0.228	0.174		0.125	0.406	
	ε_{zz} (%)	−0.203	−0.154		−0.111	−0.360	

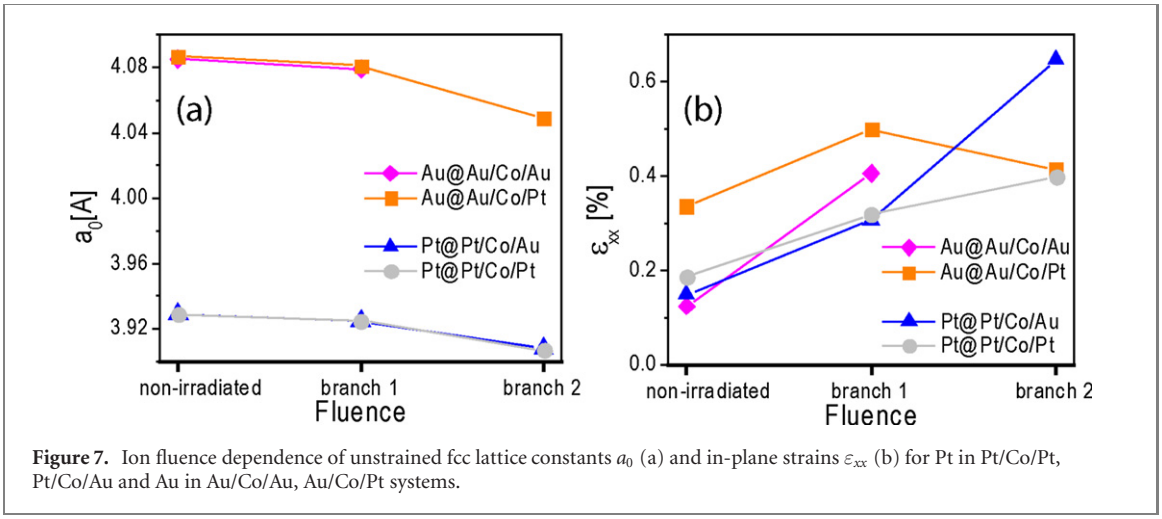

Figure 7. Ion fluence dependence of unstrained fcc lattice constants a_0 (a) and in-plane strains ε_{xx} (b) for Pt in Pt/Co/Pt, Pt/Co/Au and Au in Au/Co/Au, Au/Co/Pt systems.

The in-plane tensile strain in as-deposited films is at the level of 0.1%–0.3%. Irradiation leads to further increase with a fluence of in-plane strain developing in the buffer layers which are in a direct contact with Co layer. Qualitative agreement between fluence-dependent magnetic anisotropy field H_{1EFF} (figure 2) and in-plane strains ε_{xx} (figure 7(b)) can be found for branch 1 irradiation: the relative increase of tensile strain correlates with relative increase of magnetic anisotropy field H_{1EFF}. The effect of further increase of fluence to branch 2 does not lead to an unambiguous increase of ε_{xx}—in the case of Au/Co/Pt sample in-plane strain is reduced but still bigger than for non-irradiated sample. Here, it should be noted that for 20 nm thick buffers XRD signal mainly originates from the buffer material where Ga^+ ions are deposited, while magnetic signal originates from the volume of Co layer, where ion deposition is relatively small. Thus, two factors influence magnetic anisotropy. Firstly, residual in-plane tensile strain ∼0.2% was evaluated as an average value for rather thick bottom buffers. One can expect that in thin Co layer which is placed closer to the surface, the residual strain can be significantly bigger (∼1%) [10]. Secondly, for Co–Pt system magnetostriction coefficient depends on composition [50]. Spreading of cobalt interfaces and chemical nature of buffer/capping layers are important, too.

3.4. Positron annihilation spectroscopy

The influence of irradiation fluence on vacancy distribution and their atomic surrounding (elemental decoration of the annihilation site) were studied with positron annihilation spectroscopy (PAS), which provides crucial defect-structural characteristics of multilayer interfaces. Details about the technique itself are given in the section S2 of supplementary material. In general, positrons are extremely sensitive to the local (still volumetric) vacancy like defect concentration as well as to the electronic structure of elements surrounding of these positron trapping centers [51] and were used successfully to study other magnetic layers like FeAl [26] or Co_3O_4 [52]. We will show that the analysis and discussion of PAS results, although not as quantitative as calculations and modeling given in previous sections, provides an interpretation in line to the other structural techniques. Moreover, in our opinion it serves as an alternative and complimentary method to investigate ordering and mixing processes in multilayers. It is important to note, that implanted into a film positrons are mostly thermalized (having negligible momentum) and as a consequence of annihilation with electrons the distribution of electrons momenta is obtained, providing sensitivity to the defect size, concentration (valence—low momentum electrons), and chemical surrounding of a defect site (core—high momentum electrons).

Let us consider the dependences $S(E_p)$ in figure 8. The S parameter represents positron annihilation with low momentum valence electrons, hence it is directly proportional to open volume defect concentration and/or defect size. Here, it is combined with cDB spectroscopy analysis (section S2 in supplementary material), which is sensitive to defects elemental surrounding. The first decay of the $S(E_p)$ dependence ($E_p = 0$–2 keV) corresponds to the Pt (Au) surface layer (figure 8), whereas the raise at $E_p \approx 3$ keV represents the influence of Co layer, followed by a monotonic decrease (due to remaining buffer layers and the substrate). The existence of maximum at $E_p \approx 3$ keV indicates relatively large defect concentration around the cobalt layer particularly at its interfaces, likely due to MBE deposition at the room temperature, which is opposite to the case of our previous investigations—deposition at elevated temperature [13]. In general, a non-monotonic $S(E_p)$ dependence is a fingerprint of a multilayer structure of the pristine samples. PAS analysis of the similar MBE-grown samples [13] shows that small vacancy complexes in $L1_0$-fct-CoPt surrounding can be a major defect type. After ion irradiation a concentration of these types of vacancies decreases for both fluences and all samples regardless of the cover materials (figure 8). For the samples with Pt as a buffer layer, the maximum at $S(E_p)$ is reduced or completely diminished (figures 8(a) and (b)), i.e. the lower ion fluence (branch 1) is sufficient already to introduce Co/Pt intermixing. Clear differences are found depending on the cover material type as well. cDB investigations (supplementary material section S2, figure S50) visualize effects of intermixing as a change in Pt abundancy around the annihilation site. A disappearance of the this type of vacancies takes place (still slight step-like peculiarity of $S(E_p)$ at $E_p \approx 4$ keV is visible, which represents two different layers of intermixed material—figures 8(a) and (b), followed by a nearly complete smoothing for the higher fluence (branch 2). Here it should be noted that 30 keV Ar^+ irradiation of similar Pt/Co/Pt trilayers [13] leads to significant difference between $S(E_p)$ dependences for the lower and higher fluences. However, ion irradiation induced interface broadening depends on mass of projectiles [53]—the bigger mass, the bigger broadening. Mass of Ga atom is approximately twice bigger than of Ar, so broadening under Ga^+ irradiation should be larger.

Summarizing, PAS findings are perfectly in-line with magneto-optical and XRR modeling, suggesting Co mixing with the cover and buffer layers. In contrast the systems with Au as a buffer layer (figures 8(c) and (d)) have conserved the non-monotonic behavior (reference sample and branch 1) and plateauing of the $S(E_p)$ dependence in the Co layer region (branch 2) after irradiation. It illustrates hindered or lower intermixing due to irradiation, which is in agreement with conclusions driven out of the other techniques presented in this manuscript. cDB analysis (figure S50 in supplementary material) demonstrated only minor changes in the amplitude of the ratio curves between the pristine and irradiated samples, hence elemental defect surrounding is unchanged. Therefore, the multilayer structure is still likely preserved. Qualitatively, the width of the maximum (figure 8) representing the general Co layer area can be used to identify the level of intermixing and sharpness of interfaces. Since, the width is smaller for the Au buffered systems more coherent interface region is expected (see XRR data figure 6 as well). Sputtering effects due to irradiation, e.g. etching of the capping layer, are visible to a certain extent in the $S(E_p)$ curves, too. In case of Au buffered systems after irradiation (figures 8(c) and (d)) the position of the maximum moves gradually closer to the surface. Alternatively, the observed movement could be a consequence of interfaces broadening or superposition of both effects. Changes in the absolute values of the S-parameter at the surface can indicate, on the other hand, what kind of material remains there after irradiation. The largest S is expected for Au, slightly lower for Pt, and the lowest for Co. The surface states in branch 1 samples remain mostly unchanged. The branch 2 fluence induces variations in the surface S-parameter, where a large drop for the Au-capped case is found, which likely represents emerging Co signal. According to TRIDYN simulations the cap layer should be mostly sputtered away for branch 2 samples.

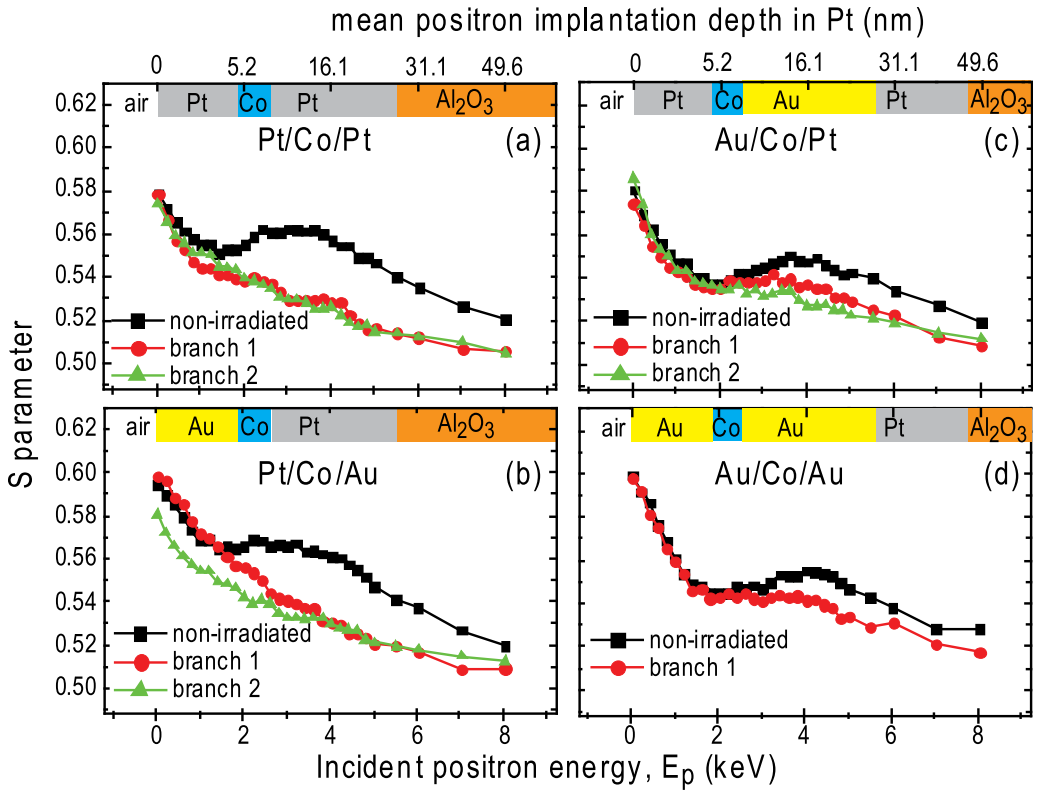

Figure 8. Low momentum fraction of electrons, *S*, as a function of positron implantation energy E_p, for different configurations of investigated trilayers: (a) Pt/Co/Pt, (b) Pt/Co/Au, (c) Au/Co/Pt, (d) Au/Co/Au. The mean implantation depth of positrons in Pt (calculated using the Makhov equation) and non-irradiated sample structures are shown at the top.

4. Conclusions

In conclusion, we have investigated the influence of adjacent Pt(Au) metals to Co magnetic layer in Pt(Au)/Co/Pt(Au) trilayers irradiated with 30 keV Ga^+ ions in the wide range of fluence *F* on its structural, magnetic, magnetooptical and properties.

Non-irradiated films with Co layer 3 nm thick are magnetized in the sample plane (negative magnetic anisotropy field H_{1EFF}). The fluence induced non-monotonic changes of magnetic anisotropy were observed in all Pt(Au)/Co/Pt(Au) structures. With increase in *F* the magnetic anisotropy first decreases for low fluence ($\sim 10^{13}$ ions cm^{-2}) being related to partial suppression of the interface anisotropy. Further fluence increase leads (except Au/Co/Au case) to creation two branches of enhanced anisotropy. Sufficiently high irradiation fluence introduces disordering that leads to change of magnetic ordering toward more isotropic state. Ion irradiation substantially affects magnetic anisotropy and especially induces PMA for Pt/Co/Pt, Pt/Co/Au and Au/Co/Pt. The type of material of cover layers, i.e. Pt or Au, influences the magnitude and monotony of magnetic anisotropy changes with fluence. The strongest changes of the amplitude of magnetic anisotropy were observed when Pt (as cap or buffer layer) was substituted by Au (Pt/Co/Au and Au/Co/Pt). Fluence induced increase of maximal value of polar Kerr rotation was observed for all Co covers containing Pt, the highest increase was found for Pt/Co/Pt structure whereas increase emerged for Pt/Co/Au and Au/Co/Pt was to less extent. On the contrary, no changes were found for Au/Co/Au.

Depth dependence of cobalt concentration in alloyed Co_xPt_{1-x} layers and/or different content of Co nanoparticles in Au layers was deduced for irradiated Pt(Au)/Co/Pt(Au) structures from: fitting of the magneto-optic complex polar Kerr effect spectra, XRR measured and TRIDYN simulations. The peak in anisotropy at branch 1 fluence correlates with irradiation-induced tensile strain. Irradiation with the high fluence (branch 2) provides partial sputtering of Co together with capping layer. Performed modeling and analyses indicate that Co mixing with cover layers occurs even for branch 1 fluence. The thickness of Au/Co interface mixing is approximately two times smaller than of Pt/Co one. The appearance of PMA magnetization for asymmetric Au/Pt covers (Au/Co/Pt and Pt/Co/Au trilayers) irradiated with branch 2 fluence can be ascribed to the stronger anisotropic behavior of CoPt alloy with Co nanodiscs [38] in the vicinity of immiscible Au layers.

PAS investigations indicate depth distribution of vacancy like defects and their atomic surrounding—a fingerprint for interfaces intermixing. We have found strong dependence of irradiation fluence on the vacancy distribution across multilayer thickness confirming interpretation given by the magnetic and structural characterization. Doppler broadening PAS can be utilized as an alternative structural technique providing qualitative analysis of ion induced ordering and mixing processes in thin films taking advantage of sensitivity to chemistry of the annihilation site.

Magnetic layer with different interfaces like Pt, Au are very attractive due to the existence of Dzyaloshinskii–Moriya interaction (DMI) [54], necessary to stabilize skyrmion structures [55]. Ion irradiation in such kind of ultrathin films allows magnetic and magnetooptical properties tuning e.g. magnetic anisotropy, coercivity field, magneto-optical parameters and probably also DMI. Thus the results of the present investigations can be applied as possible method for patterning of magnetic nanostructures required for creation of new magnonic crystals, spintronic devices.

Acknowledgments

This work was supported by FUGA (DEC-2015/16/S/ST3/00450) and Beethoven 2 (DEC-2016/23/G/ST3/04196) projects financed by the National Science Center in Poland and Charles University, project GA UK No. 1578217.

Data availability statement

The data generated and/or analysed during the current study are not publicly available for legal/ethical reasons but are available from the corresponding author on reasonable request.

ORCID iDs

P Mazalski https://orcid.org/0000-0002-7014-0901
I Sveklo https://orcid.org/0000-0002-5548-1791
Z Kurant https://orcid.org/0000-0003-0723-7310
A Wawro https://orcid.org/0000-0001-8972-9284
M O Liedke https://orcid.org/0000-0001-7933-7295
J Fassbender https://orcid.org/0000-0003-3893-9630
M Veis https://orcid.org/0000-0001-6170-7585
A Maziewski https://orcid.org/0000-0003-1154-8402

References

[1] Bland J A C and Heinrich B (ed) 1994 *Ultrathin Magnetic Structures: An Introduction to the Electronic, Magnetic and Structural Properties* vol 1 (Berlin: Springer) ch 2
[2] Franken J H, Swagten H J M and Koopmans B 2012 *Nat. Nanotechnol.* **7** 499
[3] Kim J, Lee J W, Jeong J R, Shin S C, Ha Y H, Park Y and Moon D W 2020 *Phys. Rev.* B **65** 104428
[4] Moon D W, Ha Y H, Park Y, Lee J-W, Kim J and Shin S-C 2001 *Appl. Phys. Lett.* **79** 503
[5] Chen Y J, Hwang E J and Shern C S 2008 *J. Appl. Phys.* **103** 07B516
[6] Das T, Kulkarni P-D, Purandare S C, Barshilia H C, Bhattacharyya S and Chowdhury P 2014 *Sci. Rep.* **4** 5328
[7] Chappert C *et al* 1998 *Science* **280** 1919
[8] Maziewski A *et al* 2012 *Phys. Rev.* B **85** 054427
[9] Mazalski P, Kurant Z, Maziewski A, Liedke M O, Fassbender J, Baczewski L T and Wawro A 2013 *J. Appl. Phys.* **113** 17C109
[10] Sakamaki M, Amemiya K, Liedke M O, Fassbender J, Mazalski P, Sveklo I and Maziewski A 2012 *Phys. Rev.* B **86** 024418
[11] Mazalski P *et al* 2015 *J. Synchrotron Radiat.* **22** 753
[12] Avchaciov K A, Ren W, Djurabekova F, Nordlund K, Sveklo I and Maziewski A 2015 *Phys. Rev.* B **92** 104109
[13] Jakubowski M *et al* 2019 *J. Phys.: Condens. Matter.* **31** 185801
[14] Kisielewski J, Kurant Z, Sveklo I, Tekielak M, Wawro A and Maziewski A 2016 *J. Appl. Phys.* **119** 193901
[15] Weier C *et al* 2015 *Europhys. Lett.* **109** 17001
[16] Talapatra A and Mohanty J 2016 *J. Magn. Magn. Mater.* **418** 224
[17] Massalski T 1990 *Binary Alloy Phase Diagram* (Ohio: ASM International)
[18] Harp G R, Weller D, Rabedeau T A, Farrow R F C and Toney M F 1993 *Phys. Rev. Lett.* **71** 2493
[19] Berg H and Cohen J B 1972 *Metall. Trans.* **3** 1797
[20] Ravelosona D, Chappert C, Mathet V and Bernas H 2000 *J. Appl. Phys.* **87** 5771
[21] Devolder T 2000 *Phys. Rev.* B **62** 5794
[22] Balaji S, Amirthapandian S, Panigrahi B K, Kalavathi S, Mangamma G, Gupta A, Nair K G M and Tyagi A K 2008 *Nucl. Instrum. Methods Phys. Res.* B **266** 1692

[23] Mazalski P, Kurant Z, Sveklo I, Dobrogowski W, Fassbender J, Wawro A and Maziewski A 2019 *J. Magn. Magn. Mater.* **479** 332
[24] Farrow R F C, Harp G R, Marks R F, Rabedeau T A, Toney M F, Weller D and Parkin S S P 1993 *J. Cryst. Growth* **133** 47
[25] Takai Y and Sato M 1999 *Supercond. Sci. Technol.* **12** 486
[26] Liedke M O *et al* 2015 *J. Appl. Phys.* **117** 163908
[27] Anwand W, Brauer G, Butterling M, Kissener H R and Wagner A 2012 *Defect Diffus. Forum* **331** 25
[28] Visnovsky S 1986 *Czech. J. Phys.* B **36** 834
[29] Brandle H, Weller D, Scott J C, Parking S S P and Lin C-J 1992 *IEEE Trans. Magn.* **28** 2967
[30] Visnovsky S, Nyvlt M, Parizek V, Kielar P, Prosser V and Krishnan R 1993 *IEEE Trans. Magn.* **29** 3390
[31] Visnovsky S 2006 *Optics in Magnetic Multilayers and Nanostructures* (Boca Raton, FL: CRC Press) ch 4 p 198
[32] Palik E D 1997 *Handbook of Optical Constants of Solids* (New York: Academic)
[33] Johnson P and Christy R 1974 *Phys. Rev.* B **9** 5056
[34] Aspnes D E, Theeten J B and Hottier F 1979 *Phys. Rev.* B **20** 3292
[35] Abe M and Gomi M 1984 *J. Appl. Phys.* **23** 1580
[36] Weller D, Brändle H and Chappert C 1993 *J. Magn. Magn. Mater.* **121** 461
[37] Vieu C *et al* 2002 *J. Appl. Phys.* **91** 3103
[38] Sakamaki M, Amemiya K, Sveklo I, Mazalski P, Liedke M O, Fassbender J, Kurant Z, Wawro A and Maziewski A 2016 *Phys. Rev.* B **94** 174422
[39] Möller W, Eckstein W and Biersack J P 1988 *Comput. Phys. Commun.* **51** 355
[40] Wooten F 1972 *Optical Properties of Solids* (New York: Academic)
[41] Liskova E, Veis M, Visnovsky S, Ferre J, Mougin A, Mazalski P, Maziewski A, Liedke M O and Fassbender J 2012 *Thin Solid Films* **520** 7169
[42] Jakubisova-Liskova E, Visnovsky S, Wawro A, Baczewski L T, Mazalski P, Maziewski A, Liedke M O, McCord J and Fassbender J 2014 *J. Appl. Phys.* **115** 17C106
[43] Hodgson J N 1968 *J. Phys. Chem. Solids* **29** 2175
[44] Buschow K H J 1988 *Handbook of Ferromagnetic Materials* vol 4 ed E P Wohlfarth and K H J Buschow (Amsterdam: Elsevier) p 493
[45] Weller D, Reim W, Spörl K and Brändle H 1991 *J. Magn. Magn. Mater.* **93** 183
[46] Cai M, Veres T, Schiettekatte F, Roorda S and Cochrane R W 2004 *J. Appl. Phys.* **95** 2006
[47] Sveklo I *et al* 2018 *Acta Phys. Pol.* A **133** 1215
[48] Matsunami N, Yamamura Y, Itikawa Y, Itoh N, Kazumata Y, Miyagawa S, Morita K, Shimizu R and Tawara H 1983 Energy dependence of the yields of ion-induced sputtering of monatomic solids (Institute of Plasma Physics, Nagoya University, Nagoya)
[49] Ohring M 2002 *Materials Science of Thin Films* 2nd edn (New York: Academic)
[50] Aboaf J, Herd S and Klokholm E 1983 *IEEE Trans. Magn.* **19** 1514
[51] Rehberg R and Leipner H S 1999 *Positron Annihilation in Semiconductors* (Berlin: Springer)
[52] Quintana A *et al* 2018 *ACS Nano* **12** 10291
[53] Nastasi M, Mayer J W and Hirvonen J K 1996 *Ion-Solid Interactions: Fundamentals and Applications* (*Cambridge Solid State Science Series*) (Cambridge: Cambridge University Press) ch 11
[54] Fert A, Reyren N and Cros V 2017 *Nat. Rev. Mater.* **2** 17031
[55] Wiesendanger R 2016 *Nat. Rev. Mater.* **1** 16044